



Cite this: *RSC Adv.*, 2024, **14**, 21644

Na₆MCl₈ rock-salt compounds with M = Mg, Ca, Ba, Zn, Sr as components for solid-state sodium ion batteries†

Yohandys A. Zulueta, ^a My Phuong Pham-Ho ^{bc} and Minh Tho Nguyen ^{*de}

We investigate a new series of rock-salt type structures, Na₆MCl₈ with M = Mg, Ca, Ba, Zn and Sr using advanced atomistic simulations. Calculated results show a direct relationship between the size of the M²⁺ cation and lattice parameters as well as the defect formation energy variation. The NaCl Schottky defect type is highly favourable, and the Na₆BaCl₈ structure possesses the lowest values of defect formation energies. These structures are predicted to be mechanically stable and ductile, implying their compatibility with possible use as electrodes/electrolytes. The Na₆MCl₈ structures exhibit semiconductor characteristics with an energy gap ranging between 4.1–4.6 eV, which differs from the previous value of Na₆MgCl₈. A 3D migration pathway is identified in each rock-salt structure. Despite the small variation of the Na diffusivity and conductivity at 250 K within the structures considered, the Na₆BaCl₈ is characterized by the highest conductivity at 250 K, while the Na₆MgCl₈ structure has the highest conductivity and diffusivity values. The outstanding properties predicted for a Na ion battery suggest future development of synthetic strategies for their actual preparation.

Received 14th May 2024
 Accepted 1st July 2024

DOI: 10.1039/d4ra03533j
rsc.li/rsc-advances

1. Introduction

The search for new and improved compounds for use as electrolytes and electrodes in solid-state batteries is crucial for further advancing their performance and thereby their industrial applications. Na-ion batteries are considered an effective alternative technology to the popular Li-ion batteries due to their abundance, lower cost, and eco-friendliness.^{1–9} However, their lower energy density, as compared to that of Li-ion counterparts, remains an important issue to be solved, and therefore Na batteries are not widely commercialized yet. In this context, the discovery of new compounds can help improve the energy density, safety, sustainability, and power delivery of Na-ion batteries. This will not only increase their usage in various applications such as electric vehicles, grid storage, and backup power supplies, but also contribute to the development of

sustainable energy solutions. In this context, the search for new compounds is essential for the advancement of Na-ion batteries, in particular the solid-state electrolytes (SSEs).^{1–14} The demand of conductivity for an SSE at 25 °C is $<10^{-2}$ S cm⁻¹.^{9–14} In the state-of-the-art of Na-ion battery technologies, there are not many compounds complying with this requirement, thus motivating intensive research on new materials.^{9–14} On the other hand, in order to prevent a premature device failure, an SSE must exhibit a negligible electronic and anionic conductivity, thus allowing for any undesirable reactions with the electrodes during the charge/discharge process to be avoided. Additionally, an SSE should be ductile and mechanically stable to ensure a good contact with the electrodes and prevent dendrite formation.

Solid polymers, oxide and sulphide derivatives are the most common commercial compounds used for SSEs.⁵ While oxide based SSEs tend to lead to dendrite formation and high interfacial resistance, sulphide based compounds possess a poor air stability and also high interfacial resistance.^{1–9} To overcome these problems, halide-based sodium ion conductors emerge as better candidates for solid state electrolytes having excellent electrochemical stability and high conductivity.^{8,9,15–18}

A high Na density is also required for a SSE compound, because the Na ions constitute the charge transfer source, ensuring the Na reactivity, cycling and durability. Na-rich anti-perovskite Na₃OX (X = Cl, Br) and other metal halide compounds have been studied, including the exploration of defect engineering with the aim to improve the conducting properties of defective A₃OX (A = Li⁺, Na⁺, X = Cl⁻, Br⁻)

^aDepartamento de Física, Facultad de Ciencias Naturales y Exactas, Universidad de Oriente, CP 90500, Santiago de Cuba, Cuba

^bFaculty of Chemical Engineering, Ho Chi Minh City University of Technology (HCMUT), 268 Ly Thuong Kiet Street, Dist. 10, Ho Chi Minh City, Vietnam

^cVietnam National University Ho Chi Minh City, Linh Trung, Thu Duc City, Ho Chi Minh City, Vietnam

^dLaboratory for Chemical Computation and Modeling, Institute for Computational Science and Artificial Intelligence, Van Lang University, Ho Chi Minh City, Vietnam.
 E-mail: minhtho.nguyen@vlu.edu.vn

^eFaculty of Applied Technology, School of Technology, Van Lang University, Ho Chi Minh City, Vietnam

† Electronic supplementary information (ESI) available. See DOI: <https://doi.org/10.1039/d4ra03533j>



structures.^{15–18} The effects on Na ion conductivity upon doping with divalent and trivalent dopants have been explored employing atomistic simulation computations.¹⁵ Favourable incorporation mechanisms have been found to increase the Na vacancy concentration with effective effect on the Na conductivity.¹⁸ The Na⁺ conductivity in the chloride Na₃OCl amounts to 10^{−7} S cm^{−1} at 300 K.¹⁸ On the other hand, a theoretical study demonstrated that Na₃YCl₆ and Na₃Y₂Cl₉ compounds are electrochemically stable with outstanding transport properties.⁷ Other promising halides such as NaAlCl₄, Na_{3−x}Er_{1−x}Zr_xCl₆, Na_{2+x}Zr_{1−x}In_xCl₆, Na₂ZrCl₆ and Na_{3−x}Y_{1−x}Zr_xCl₆ have been synthesized, with the higher Na ionic conductivities of ~10^{−5} S cm^{−1}.^{6,19–22}

Atomistic simulations provide us with a detailed understanding of the mechanisms that govern the properties of battery materials.^{23–25} Such a understanding is necessary for selection on the composition, crystal structure, and defect properties of the material. Simulations can also predict stability and reactivity with different electrolytes, particularly their electrochemical behaviour leading to better performance. Overall, atomistic simulations have been proved to be a powerful approach for materials design and discovery, essential for developing new and improved battery materials.^{15,23–27}

In our previous work, advanced atomistic simulations have been used to evaluate the main properties of the Na₆MgCl₈ rock-salt material.²⁷ The Na₆MgCl₈ has an insulating characteristic with an energy gap of 5.1 eV and is mechanically stable and ductile. Our simulations also predicted that the Zn²⁺ ion is the best divalent dopant, improving the defect characteristics and transport properties of Na₆MgCl₈. Na transport properties are significantly improved following doping of the Na₆MgCl₈ with the divalent Ba²⁺ and Zn²⁺ ions.²⁷ Considering that the Zn²⁺, Ca²⁺, Sr²⁺ and Ba²⁺ ions are doubly charged as the Mg²⁺ cation, we set out to further explore the main properties of a new series of rock-salt structures, namely the Na₆MgCl₈ with divalent M²⁺ cations being Mg²⁺, Ca²⁺, Ba²⁺, Zn²⁺ and Sr²⁺, using advanced atomistic simulations. Structural, electronic and mechanical properties, including intrinsic defects formation and transport properties are investigated. Our simulation results suggest some novel compounds for subsequent experimental preparations and verifications to evaluate their potential application as electrolytes.

2. Computational methodology

Density functional theory (DFT) calculations are carried out using the CASTEP code,²⁸ to explore the structural, electronic spectroscopy and mechanical properties of Na₆MgCl₈ structure. We adopt the setup described in our previous work on Na₆MgCl₈.²⁷ DFT calculations are performed using the generalized gradient approximation (GGA) with the Perdew–Burke–Ernzerhof exchange–correlation functional optimized for solid (PBE-SOL).²⁹ The pseudoatomic functions for Na-2s²2p⁶3s¹, M-2p⁶3s² and Cl-3s²3p⁵ in the reciprocal representations are used to represent the electronic configuration of the constituent atoms in these structures. The convergence thresholds for self-consistent computation, and geometry optimization

calculations are taken with a total energy change of 5 × 10^{−6} eV per atom, and maximum force, stress and atomic displacements of 10^{−2} eV Å^{−1}, 2 × 10^{−2} GPa and 5 × 10^{−4} Å, respectively. Ultrasoft pseudopotentials with a plane-wave energy cut-off of 830 eV are adopted. A 4 × 4 × 4 *k*-point set along the Monkhorst–Pack scheme which is used to sample the Brillouin zone during the geometry optimization.³⁰

The General Utility Lattice Program (GULP) is used to perform force field-based computations.³¹ The potential (force field) parameters are taken from previous studies.^{15,27,32} The Buckingham approximation is used for the short-range interactions, while long-range interactions are treated as coulombic interactions where only the charge and the interatomic distance describe the long-range potential energy. The Dick–Overhauser model is included for consideration of the ionic polarization where each ion is approximated as a positively charged core and a negatively charged shell linked by a spring (with spring constant *k*), and the sum of the core–shell charge results in the formal charge (*Z*) of the polarizable species.³³

The Mott–Littleton method is used for the defect calculations in which the crystal structure is divided into two concentrically spherical regions with the radius of *R*₁ and *R*₂ with *R*₁ < *R*₂.³⁴ At the inner sphere, the isolated defect, or defect cluster, is positioned where the interaction between the defect(s) with the local structure is strong, while the region *R*₂ is treated by a quasi-continuum approximation.³⁴ Values of *R*₁ = 13 Å and *R*₂ = 27 Å are adopted, ensuring a smooth convergence of the simulations. The Broyden–Fletcher–Goldfarb–Shanno algorithm is used for geometry optimizations and defect energetics computations.^{31,35} This technique has extensively been used to explore the defect formation in different types of solid-state materials.^{17,23–27}

The bond valence method is a simple and effective approach for determining the diffusion paths and activation energies for diffusion and conduction.^{21,36–38} This method identifies the mobile cation with regions of low bond valence site energy. The bond length between a cation A and an anion, denoted as X (*L*_{A–X}), is evaluated with the help of tabulated empirical parameters *L*_{0,A–X} and *b*_{A–X}, and it is related to an individual bond valence (eqn (1)):

$$S_{A-X} = \exp[(L_{0,A-X} - L_{A-X})/b_{A-X}] \quad (1)$$

By adding the coulombic repulsive term (*E*_{repulsion}) of the mobile A ion respect to other immobile ions, the bond valence site energy of a cation A [*E*_{BVSE}(A)] is evaluated in a similar way to the Morse empirical potentials:^{36–40}

$$E_{BVSE}(A) = \sum_X D_0 \left[\sum_{i=1}^N \left[(S_{A-X}/S_{\min,A-X})^2 - 2S_{A-X}/S_{\min,A-X} \right] \right] + E_{\text{repulsion}} \quad (2)$$

The bond valence pathway analyser (softBV-GUI) code is used for the computation *E*_{BVSE} and the required parameters in eqn (2) are included in the code.⁴⁰ For the analysis of the



$E_{\text{BVSE}}(\text{Na})$, while coulombic repulsions are considered between mobile Na and immobile M^{2+} cations, coulombic attraction interactions are included into the Morse type attraction terms. Further details on the bond valence approach can be found in ref. 36–40.

3. Results and discussion

3.1. Structural characterization and defect energetics of Na_6MCl_8 ($\text{M}^{2+} = \text{Mg}^{2+}, \text{Zn}^{2+}, \text{Ca}^{2+}, \text{Sr}^{2+}, \text{Ba}^{2+}$)

Fig. 1 displays the unit cell of these compounds in their primitive and conventional representations. On the basis of the Na_6MgCl_8 structure, the proposed Na_6MCl_8 ($\text{M}^{2+} = \text{Zn}^{2+}, \text{Ca}^{2+}, \text{Sr}^{2+}, \text{Ba}^{2+}$) compounds consist in a rock-salt structure with four Z formula units in the cubic $Fm\bar{3}m$ space group; the M^{2+} ion is bonded to six equivalent Cl^- atoms forming $[\text{MCl}_6]$ octahedron, while the Na^+ cations are 6-coordinated with Cl^- anions sharing corners and edges with $[\text{MCl}_6]$ and $[\text{NaCl}_6]$ octahedra.

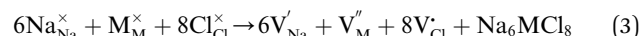
To explore the lattice properties of Na_6MCl_8 ($\text{M}^{2+} = \text{Mg}^{2+}, \text{Zn}^{2+}, \text{Ca}^{2+}, \text{Sr}^{2+}, \text{Ba}^{2+}$), the lattice energies of NaCl and MCl_2 compounds are computed. In what follows, the Na_2MgCl_8 results previously reported in ref. 27 are included for a direct comparison of the structures considered. Following the computational protocol implemented in our previous work,^{24,27} the Na-, M- and Cl-vacancy energies (V'_{Na} , V''_{M} and V'_{Cl} respectively) are computed. Table 1 collects the results for lattice parameters and basic defect formation of Na_6MCl_8 . Inclusion of the ionic radius of M^{2+} in Table 1 serves to clarify the tendency

of the lattice energy and cell parameters in response to changes in ionic size.

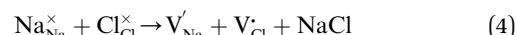
As it is shown, the lattice energy of constituent chlorides and Na_6MCl_8 ($E_{\text{L}}^{\text{MCl}_2}, E_{\text{L}}^{\text{NaCl}}$ and $E_{\text{L}}^{\text{Na}_6\text{MCl}_8}$), cell parameters and vacancy formation energies tend to decrease with increasing ionic radius. Another point of interest is that Na vacancy formation is associated with the lowest energy followed by the Cl vacancy energy. Various reports of such energetic behaviour subtend that both Na and Cl vacancies are the most abundant defect type in other Na–Cl containing materials.^{15,18,27} A clear influence of M^{2+} ionic radius on the lattice properties and vacancy formation is thus demonstrated. As the ionic radius increases, the lattice parameters of MCl_2 and Na_6MCl_8 structures increase whereas the rest of the magnitude decrease.

Results of the interatomic distances (d) of each Na_6MCl_8 structure emphasize that the central cation size affects the Na–Na ($d_{\text{Na–Na}}$) distance, which in turn determines the diffusion properties of these materials.²⁷ The $d_{\text{Na–Na}}$ value decreases in going from Na_6MgCl_8 to Na_6ZnCl_8 and increase to 4.09 Å in Na_6BaCl_8 . Several Na-containing structures currently considered in battery technologies exhibit similar Na–Na interatomic distances to those observed in the present Na_6MCl_8 compounds.^{15,19,20}

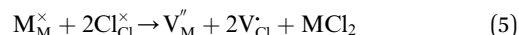
Along with the results of basic defects formation, the intrinsic defects play an important role determining the transport properties of materials. In particular, the Schottky defect type is the most common defect scheme present in conducting materials. The Schottky formation mechanism is usually described in terms of three different schemes; the first scheme can be written in the Kröger–Vink notation,⁴¹ as expressed by eqn (3):



where $\text{Na}_{\text{Na}}^{\times}$, $\text{M}_\text{M}^{\times}$ and $\text{Cl}_{\text{Cl}}^{\times}$ represent the host ions occupying its respective atomic position at the Na_6MCl_8 lattice structure, while V'_{Na} , V''_{M} and V'_{Cl} symbolize a Na, M and Cl-vacancy, respectively. In the present context, eqn (3) describes the full Schottky defect formation mechanism, in which formation of NaCl Schottky defect can be described by eqn (4):



leading to the stoichiometric $\text{Na}_{6-x}\text{MCl}_{8-x}$ composition, while the formation of MCl_2 Schottky defect is given by eqn (5):



which leads to the stoichiometric $\text{Na}_6\text{M}_{1-x}\text{Cl}_{8-2x}$ formula. As in our previous work, the Frenkel type defects are not considered because they are usually energetically unfavorable.^{18,24}

According to the defect-energetics computation protocols used in a previous work, the solution energy (E_s) is computed as follows (eqn (6)–(8)):

$$E_s = \frac{1}{3} (6E_{\text{vac}}^{\text{Na}} + E_{\text{vac}}^{\text{M}} + 8E_{\text{vac}}^{\text{Cl}} + E_{\text{L}}^{\text{Na}_6\text{MCl}_8}) \quad (6)$$

$$E_s = \frac{1}{2} (E_{\text{vac}}^{\text{Na}} + E_{\text{vac}}^{\text{Cl}} + E_{\text{L}}^{\text{NaCl}}) \quad (7)$$

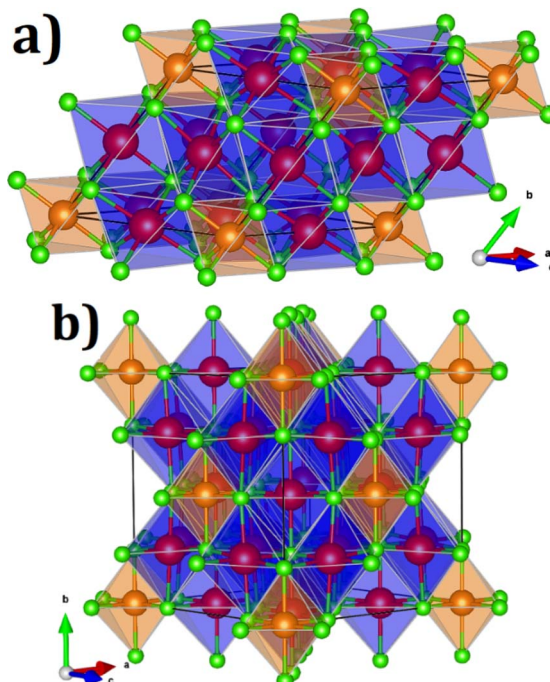


Fig. 1 (a) Primitive and (b) conventional representations of Na_6MCl_8 lattice structures (space group $Fm\bar{3}m$). Blue and green balls represent the Na^+ and Cl^- ions and orange and blue polyhedral represent the $[\text{MCl}_6]$ and $[\text{NaCl}_6]$ octahedra, respectively.



Table 1 Basic defect formation energies and interatomic distances of Na_6MCl_8 structures

(a) Na_6MCl_8	M^{2+}	IR (CN VI)	$E_{\text{L}}^{\text{MCl}_2}$	a (Å)	$E_{\text{vac}}^{\text{Na}}$	$E_{\text{vac}}^{\text{M}}$	$E_{\text{vac}}^{\text{Cl}}$	$E_{\text{L}}^{\text{Na}_6\text{MCl}_8}$
Na_6MgCl_8	Mg	0.72	-26.52	11.085	5.181	21.765	5.435	-75.255
Na_6ZnCl_8	Zn	0.74	-26.93	11.049	5.183	22.515	5.472	-76.112
Na_6CaCl_8	Ca	0.99	-21.15	11.420	5.007	16.264	5.081	-69.094
Na_6SrCl_8	Sr	1.18	-21.14	11.440	4.984	15.911	5.058	-68.735
Na_6BaCl_8	Ba	1.35	-20.16	11.564	4.815	14.130	4.917	-66.983

(b) Interatomic distance (in Å)	Na_6MCl_8				
	Na_6MgCl_8	Na_6ZnCl_8	Na_6CaCl_8	Na_6SrCl_8	Na_6BaCl_8
$d_{\text{Cl-Cl}}$	3.456	3.392	4.017	4.043	3.957
$d_{\text{Na-Na}}$	3.919	3.906	4.038	4.045	4.088
$d_{\text{M-M}}$	7.838	7.813	8.075	8.090	8.177
$d_{\text{Cl-Na}}$	2.785	2.762	2.855	2.860	2.892
$d_{\text{Cl-M}}$	2.443	2.399	2.840	2.862	2.984
$d_{\text{M-Na}}$	3.919	3.906	4.038	4.045	4.088

(c) Schottky formation energy (eV per defect)					
Na_6MCl_8	M^{2+}	IR (CN VI)	NaCl Schottky	MCl_2 Schottky	Na_6MCl_8 Schottky
Na_6MgCl_8	Mg	0.72	1.26	3.06	7.03
Na_6ZnCl_8	Zn	0.74	1.28	3.27	7.09
Na_6CaCl_8	Ca	0.99	0.99	2.64	5.96
Na_6SrCl_8	Sr	1.18	0.97	2.44	5.85
Na_6BaCl_8	Ba	1.35	0.82	1.90	5.12

$$E_s = \frac{1}{2} (E_{\text{vac}}^{\text{M}} + 2E_{\text{vac}}^{\text{Cl}} + E_{\text{L}}^{\text{MCl}_2}) \quad (8)$$

in relation with eqn (3)–(5), respectively; where $E_{\text{vac}}^{\text{Na}}$, $E_{\text{vac}}^{\text{M}}$, and $E_{\text{vac}}^{\text{Cl}}$ denotes the Na-, M- and Cl-vacancy energy, while $E_{\text{L}}^{\text{Na}_6\text{MCl}_8}$, $E_{\text{L}}^{\text{NaCl}}$ and $E_{\text{L}}^{\text{MCl}_2}$ represent the lattice energy of Na_6MCl_8 , NaCl and MCl_2 compounds, respectively.

The results of basic defect formation energies are also included in Table 1. For the three Schottky defects type considered, the solution energies decrease with respect to the increment of the M^{2+} ionic radius. The most favorable Schottky defect formation corresponds to the NaCl in all structures, followed by the MCl_2 , and the unfavorable Na_6MCl_8 Schottky. In addition, within the Schottky defect type, the Na_6BaCl_8 structure has the lowest values of defect formation energy. Taking now a closer look into the M^{2+} ionic radius and the defect energetics behaviour, we note that the lattice parameters from Na_6MgCl_8 to Na_6ZnCl_8 decrease and gradually increases for the rest of structures considered. As was discussed before,²⁷ a similar behavior upon the M^{2+} ionic radius is found for the interatomic distances. The behavior of the defect energetics is similar to those disclosed for the lattice parameters and interatomic distances. These results can be attributed to the increase in the average bond length and volume of the $[\text{MCl}_6]$ octahedron, which in turn affects the corresponding bond length and volume of the $[\text{NaCl}]$ octahedron. This effect occurs with the increment of the M^{2+} ionic radius. These results point out a direct relationship between the M^{2+} ionic radius with the defect chemistry within the Na_6MCl_8 framework, including the

aforementioned relation to the lattice parameters and interatomic distances.

Fig. 2 shows the band structure of Na_6MgCl_8 in which the Fermi level is taken as the 0 eV reference. The valence bands are located in the range of -3 eV and the Fermi level, and the conduction bands lies between 4.5 and 17 eV. The energy gap

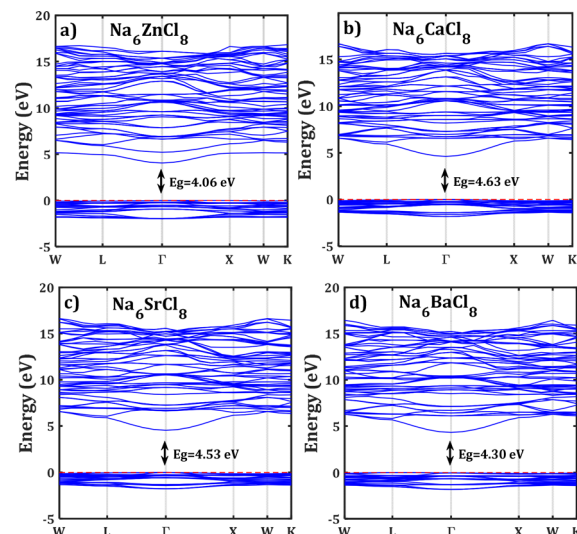


Fig. 2 Band structure of the Na_6MCl_8 ($\text{M} = \text{Zn, Ca, Sr, Ba}$). The computed energy gap (E_g) are shown in each case. Horizontal red line represents the Fermi level.



values are included in figures; these values are remarkably lower than that of 5.1 eV reported for Na_6MgCl_8 structure.²⁷ In this sense, the new compound inherits the electronic characteristics of the Na_6MgCl_8 partner structure, in which many electrons are present at the top valence bands at the Γ -point. This aligns well with the criteria for consideration of SSEs, as these compounds possess a minimal electronic conduction. However, it is crucial to exercise caution while interpreting the computed energy gap due to the characteristic tendency of DFT computations to underestimate the band gaps and the absence of experimental results for calibration.⁴²

3.2. Mechanical stability

Exploration of mechanical properties is of great importance when choosing materials to be used as electrode or electrolyte in batteries.^{43–45} The key requirements for mechanical stability include moderate Young modulus in order to ensure optimal contact between a solid electrolyte and the electrodes, thus avoiding the presence of undesirable voids and cracks affecting the long range transport properties.^{43–45}

The mechanical response of a crystalline structure is described by the Hooke law, and expressed by the elastic constant matrix (C_{ij}), defined as in eqn (9):

$$C_{ij} = \frac{1}{V_0} \left(\frac{\partial^2 E}{\partial \varepsilon_i \partial \varepsilon_j} \right) \quad (9)$$

where E represents the total energy, V_0 its equilibrium volume and ε the strain load.⁴⁶ From eqn (9), the total energy (E) is given by eqn (10):

$$E = E_0 + \frac{V_0}{2} \sum_{i,j=1}^6 C_{ij} \varepsilon_i \varepsilon_j + O(\varepsilon^3) \quad (10)$$

where the zero subscript is referred to the equilibrium state of the crystal and $O(\varepsilon^3)$ is an infinitesimal of the strain load of order 3. The Born criteria establishes the mechanical stability condition by stating that the energy for a homogeneous deformation loaded by an infinitesimal strain must be positive.⁴⁶ In other words, the C_{ij} matrix should be positive definite, inferring positive eigenvalues (λ) and its quadratic form satisfies the Hooke law.⁴⁶ The eigenvalues in the cubic symmetry satisfy the following relations (11):

$$\begin{cases} \lambda_1 = \lambda_2 = \lambda_3 > 0; \quad \lambda_4 = \lambda_5 > 0; \\ \lambda_6 > 0 \text{ such as } \lambda_1 \neq \lambda_4, \quad \lambda_6 \neq \lambda_1, \quad \lambda_6 \neq \lambda_4 \end{cases} \quad (11)$$

The C_{ij} matrix elements of each compound are collected in the ESI file.† All the C_{ij} values are positive. Moreover, the values of C_{44} , C_{55} and C_{66} are significantly lower than the diagonal C_{ij} ($i,j = 1, 2, 3$); elements for all Na_6MCl_8 structures, which implies that a shear deformation is more probable to occur as a consequence of the strong resistance to uniaxial stress.^{46–54} Shear deformations had been observed in other battery materials with consequences in their performances.^{46–54} Table 2 collects the computed eigenvalues of each Na_6MCl_8 structure considered, including those obtained in our previous work for Na_6MgCl_8

Table 2 Eigenvalues and other mechanical properties (in GPa) of compounds considered

(a) Compound	λ_1	λ_4	λ_6
Na_6MgCl_8	13.74	34.81	79.72
Na_6ZnCl_8	13.92	35.75	82.28
Na_6CaCl_8	12.43	25.16	59.72
Na_6SrCl_8	12.36	24.47	58.66
Na_6BaCl_8	11.91	20.50	53.01

(b)	Mechanical properties	Reuss	Voigt	Hill
Na_6MgCl_8	B	26.574	26.574	26.574
	G	15.004	15.206	15.105
	$E(x,y,z)$	42.860	42.860	42.860
	B/G	1.771	1.748	1.759
	Compressibility	0.038		
Na_6ZnCl_8	B	27.426	27.426	27.426
	G	15.270	15.500	15.385
	$E(x,y,z)$	44.053	44.053	44.053
	B/G	1.796	1.769	1.783
	Compressibility	0.036		
Na_6CaCl_8	B	19.906	19.906	19.906
	G	12.490	12.490	12.490
	$E(x,y,z)$	31.175	31.175	31.175
	B/G	1.594	1.594	1.594
	Compressibility	0.050		
Na_6SrCl_8	B	19.555	19.555	19.555
	G	12.311	12.311	12.311
	$E(x,y,z)$	30.367	30.367	30.367
	B/G	1.588	1.588	1.588
	Compressibility	0.051		
Na_6BaCl_8	B	17.670	17.670	17.670
	G	11.186	11.246	11.216
	$E(x,y,z)$	25.771	25.771	25.771
	B/G	1.580	1.571	1.575
	Compressibility	0.057		

structure.²⁷ All the eigenvalues are positive revealing that these structures are mechanically stable. Besides, in all cases $\lambda_1 < \lambda_4 < \lambda_6$ and the same trend of λ_i values is observed upon the increment of M^{2+} ionic size (from Mg^{2+} to Zn^{2+} the λ_i increases and decreases from Zn^{2+} to Ba^{2+}). This means that the central ionic size (*i.e.* the ionic radius of M^{2+} in the Na_6MCl_8 lattice structures) induces direct implications elucidating the mechanical stability.

To our knowledge, no report is actually available concerning the relation of λ_i absolute value with mechanical stability. In addition, as the λ_i depends on the C_{ij} , and in considering eqn (11), we note the ordering relation $\lambda_1 < \lambda_4 < \lambda_6$ which is an expression of high probability of shear deformation because of strong resistance to a uniaxial deformation. This criterion (*i.e.*, $\lambda_1 < \lambda_4 < \lambda_6$) can be used in other compounds with similar space group to elucidate shear deformation characteristics.

With the computed C_{ij} elements, the bulk, shear, and Young modulus values are obtained by using the individual and polycrystalline Voigt–Reuss–Hill approximations. The formulations describing the relevant magnitudes can be found elsewhere.^{50–54} Table 2 includes the bulk (B), shear (S), Young modulus (E), B/G



and compressibility of each compound. These parameters provide us with a support for the mechanical stability in relation with an external force inducing volume change and ductility of compounds. As it is shown, these magnitudes follow the same behaviour encountered before upon the variation of the ionic radius. The highest value of Young modulus of 44 GPa and the lowest value of 26 GPa correspond to those of Na_6MgCl_8 and Na_6BaCl_8 , respectively. The values of Young modulus are comparable to those of available battery materials.

The Pugh's formula (B/G) establishes the limit of a material to be considered as ductile or brittle.⁵⁴ The Na_6ZnCl_8 appears to be the most ductile material followed by Na_6MgCl_8 ($B/G > 1.75$). The B/G values of other compounds remain at ~ 1.6 , indicating

that they can be classified as partially ductile compounds. In summary, the Na_6MCl_8 compounds are mechanically stable having appropriate mechanical properties, thus promoting them as applicable battery materials.

3.3. Transport properties of Na_6MCl_8 ($\text{M} = \text{Ca}^{2+}, \text{Ba}^{2+}, \text{Zn}^{2+}$ and Sr^{2+})

Transport properties such as diffusion and conduction mechanisms are explored by using the BV method. The Na^+ diffusion coefficient and conductivity within the electrode/electrolyte material determines the sodiation/desodiation rate during the charge/discharge cycles.¹⁻⁵ In this sense, exploration of transport properties of emerging materials is essential for achieving

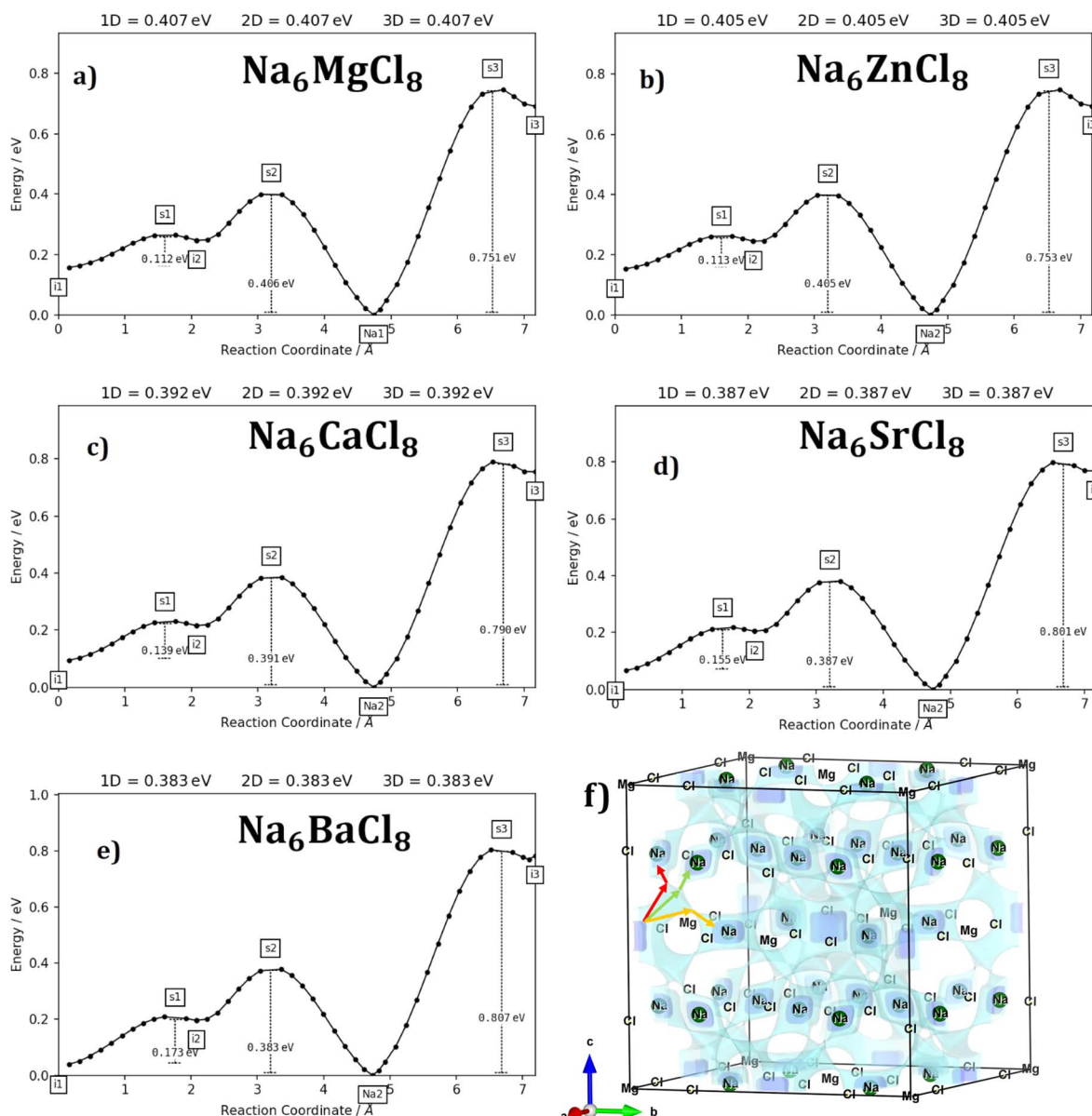


Fig. 3 Energy vs. reaction coordinate profiles of Na_6MCl_8 with $\text{M} = \text{Ca}^{2+}, \text{Ba}^{2+}, \text{Zn}^{2+}$ and Sr^{2+} , (a) Na_6MgCl_8 , (b) Na_6ZnCl_8 , (c) Na_6CaCl_8 , (d) Na_6SrCl_8 , (e) Na_6BaCl_8 , (f) 3D network of Na^+ pathways in Na_6MgCl_8 (blue isosurfaces) calculated by bond valence site energy. In (f) the rest Na_6MCl_8 structures the migration pathway isosurfaces are similar, and the arrows highlight the Na^+ migration pathways.



high energy density, high power output, and long cycle life in Na-ion batteries, particularly for emerging applications such as electric vehicles and grid-scale energy storage.

Following the approaches described in ref. 40, the first step deals with an exploration of the migration path derived from the bond valence site energy. Migration paths for Na^+ ions contemplate regions of low bond valence site energy in mesh grids covering the Na_6MCl_8 structure models with a resolution of $\pm 0.1 \text{ \AA}^3$.

Fig. 3a–e displays the energy variation against the reaction coordinate of each Na_6MCl_8 ($\text{M} = \text{Ca}^{2+}$, Ba^{2+} , Zn^{2+} and Sr^{2+}) structure. Fig. 3f depicts the energy surface describing the Na^+ migration pathways into the Na_6MgCl_8 . The isosurfaces of remaining Na_6MCl_8 structures are quite analogous to each other. Three 3D migration paths are found within each Na_6MCl_8 structure. Three saddle points (transition structures) are identified in all structures (denoted as s_1 , s_2 and s_3). Interstitial mechanism described by a Na Frenkel defect type $\text{Na}_{\text{Na}}^{\text{x}} \rightarrow \text{V}_{\text{Na}} + \text{Na}_i^{\text{+}}$ appears as the scheme describing the migration mechanism. In addition, three favourable interstitial sites are also identified, namely i_1 , i_2 and i_3 , in these structures.

In Na_6MCl_8 compounds, variations in bond length and the $\text{Na}-\text{Na}$ distance (diffusion length) occur due to changes in the M^{2+} ionic radius. As the M^{2+} ion size increases, more space becomes available between the $[\text{NaCl}]$ and $[\text{MCl}_2]$ octahedra. This increased spacing allows additional Na ions to be accommodated, resulting in a favourable interstitial mechanism. Consequently, the diffusion length is reduced, leading to improved overall Na transport properties.

Fig. 4 collects the transport properties namely the conducting behaviour and relevant information concerning the diffusivity and conductivity at 250 K of all structures studied. The

Arrhenius dependence of Na conductivity is observed in all samples. The calculated activation energy lies in the range of 0.38–0.41 eV in going from Na_6BaCl_8 to Na_6MgCl_8 structures. While the lowest E_a value corresponds to Na_6BaCl_8 , the Na_6MgCl_8 structure has the highest one. Bearing in mind the ionic size of M cations, we can note the same behaviour of inverted proportionality of E_a against ionic radius.

The conductivity data are derived following the Nernst–Einstein equation in which the diffusion coefficient at each temperature is directly proportional with the conductivity of the mobile ion.^{15,23–25} In this case, the same E_a value obtained by BVSE method is used to derive the conductivity using the softBV-GUI computer code.⁴⁰

From Fig. 4c and d, it can be observed that the highest value of Na^+ conductivity and diffusivity at 250 K ($\sigma_{250 \text{ K}}$ and $D_{250 \text{ K}}$, respectively) are found in the Na_6BaCl_8 structure, with values of $3.22 \times 10^{-6} \text{ S cm}^{-1}$ and $2.46 \times 10^{-11} \text{ cm}^2 \text{ s}^{-1}$ respectively. In contrast, the Na_6MgCl_8 structure has values of $\sigma_{250 \text{ K}} = 1.19 \times 10^{-6} \text{ S cm}^{-1}$ and $D_{250 \text{ K}} = 9.12 \times 10^{-12} \text{ cm}^2 \text{ s}^{-1}$. The E_a values of these structures comply with the requirement for battery materials. For instance, in our previous work, an activation energy of 0.45 eV and a conductivity of $7.12 \times 10^{-7} \text{ S cm}^{-1}$ of Na_3OCl solid-state electrolyte were determined.²⁷ In addition, a combined deep potential MD, *ab initio* MD and static simulations study of the Na^+ migration in Na_3OBr solid state electrolyte, reported a diffusion activation energy of 0.41–0.43 eV and a conductivity at 273 K of $2 \times 10^{-7} \text{ S cm}^{-1}$.^{15,18} In the particular case of Na_6MgCl_8 structure, we found that the Ba^{2+} doped Na_6MgCl_8 leading the stoichiometric $\text{Na}_{6-x}\text{Ba}_x\text{MgCl}_8$ promotes the Na vacancy concentration and improves the conductivity at 300 K as compared to the defective $\text{Na}_{6-x}\text{MgCl}_{8-x}$.²⁷ Surprisingly, the Na_6BaCl_8 structure exhibits the most promising transport properties, making this new compound a novel candidate for Na ion battery technology.

In summary, the Na_6MCl_8 compounds with ($\text{M} = \text{Ca}, \text{Ba}, \text{Zn}$ and Sr) structures comply with the requirements to be considered as cathode materials having favourable structural and electronic properties, mechanically stable and ductile and interesting transport properties. Besides, transport property of $<10^{-5} \text{ S cm}^{-1}$ is required to be considered as a solid-state electrolyte. Introduction of foreigner cations or designing polyanionic $\text{Na}_6\text{MCl}_{8-x}\text{A}_x$ compounds are recommendable approaches to improve their transport properties at 25 °C.

4. Concluding remarks

In this theoretical study, we explore a novel series of rock-salt type structures, Na_6MCl_8 (where $\text{M} = \text{Mg}^{2+}$, Ca^{2+} , Ba^{2+} , Zn^{2+} , and Sr^{2+}), using advanced atomistic simulations. Our investigation focuses on their structural, electronic, and mechanical properties, including defect energetics and transport behaviour, with the goal of understanding their potential application in solid-state sodium-ion battery technology.

The key findings include a direct correlation between the ionic size of the divalent M^{2+} cation and lattice parameters, as well as defect formation energy variations. As the M^{2+} cation

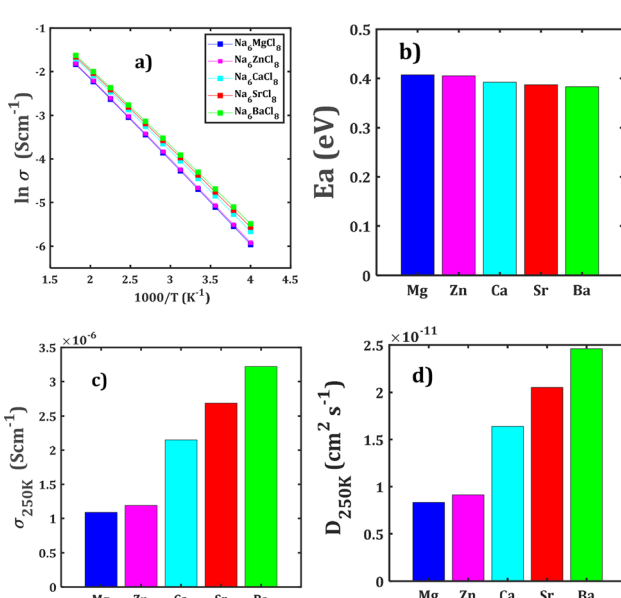


Fig. 4 (a) Arrhenius dependence of Na conductivity (σ) with the temperature (T) of Na_6MCl_8 structures, (b) their respective activation energy (E_a), (c) conductivity ($\sigma_{250 \text{ K}}$) and (d) diffusivity ($D_{250 \text{ K}}$) at 250 K.



size increases, lattice parameters, interatomic distances, and defect energies tend to decrease. The NaCl Schottky defect type is particularly favourable, and the Na_6BaCl_8 structure exhibits the lowest defect formation energy. The low defect formation energies determined in this work indicate that these materials can accommodate defects without compromising their stability, which is of crucial importance for any long-term battery operation.

Mechanical stability and ductility characterize these structures, suggesting a possible compatibility for both electrodes and electrolytes for Na-ion batteries. The Na_6MCl_8 compounds exhibit insulating properties, with an energy gap ranging from 4.1 to 4.6 eV, different from the reported value for Na_6MgCl_8 (5.1 eV). The energy gap within the Na_6MCl_8 compounds suggests their potential as solid-state electrolytes, allowing an efficient Na^+ transport while preventing an electronic conduction.

The transport properties of Na_6MCl_8 compounds are disclosed by the bond valence site energy approach for rapid predictions. A 3D migration pathway is identified in each rock-salt structure. The corresponding activation energy lies in the range of 0.38–0.41 eV in going from Na_6BaCl_8 to Na_6MgCl_8 structures. Despite the small variation of the Na conductivity and diffusivity at 250 K within the structures considered, the Na_6BaCl_8 is characterized by the highest conductivity and diffusivity at 250 K of $3.22 \times 10^{-6} \text{ S cm}^{-1}$ and $2.46 \times 10^{-11} \text{ cm}^2 \text{ s}^{-1}$, respectively, while the Na_6MgCl_8 structure has respective values of $1.19 \times 10^{-6} \text{ S cm}^{-1}$ and $9.12 \times 10^{-12} \text{ cm}^2 \text{ s}^{-1}$. The Na_6MCl_8 structures, especially Na_6BaCl_8 , show promising ionic conductivity. Their ability to facilitate the Na^+ migration can greatly enhance the battery performance.

We hope that these outstanding predicted properties motivate following experimental syntheses and investigations of Na_6MCl_8 compounds, leading to practical applications in the current and future solid-state Na-ion batteries.

Data availability

The data supporting this article have been included as part of the ESI.†

Author contributions

YAZ: conception, data acquisition and interpretation, original draft preparation, editing, review. MPPH: data analysis, editing, review. MTN: conception, project supervision, manuscript editing and review. All authors reviewed the manuscript.

Conflicts of interest

There are no conflicts to declare.

Acknowledgements

MPPH acknowledges Ho Chi Minh City University of Technology (HCMUT) and Viet Nam National University VNU-HCM for supporting this study.

Notes and references

- Y. Deng, C. Eames, L. H. B. Nguyen, O. Pecher, K. J. Griffith, M. Courty, B. Fleutot, J. N. Chotard, C. P. Grey, M. S. Islam and C. Masquelier, *Chem. Mater.*, 2018, **30**, 2618–2630.
- H. Tian, S. Liu, L. Deng, L. Wang and L. Dai, *Energy Storage Mater.*, 2021, **39**, 232–238.
- K. Chayambuka, G. Mulder, D. L. Danilov and P. H. L. Notten, *Adv. Energy Mater.*, 2018, **8**, 1–49.
- Y. Wang, S. Song, C. Xu, N. Hu, J. Molenda and L. Lu, *Nano Mater. Sci.*, 2019, **1**, 91–100.
- J. A. S. Oh, L. He, B. Chua, K. Zeng and L. Lu, *Energy Storage Mater.*, 2021, **34**, 28–44.
- E. A. Wu, S. Banerjee, H. Tang, P. M. Richardson, J. M. Doux, J. Qi, Z. Zhu, A. Grenier, Y. Li, E. Zhao, G. Deysher, E. Sebti, H. Nguyen, R. Stephens, G. Verbiest, K. W. Chapman, R. J. Clément, A. Banerjee, Y. S. Meng and S. P. Ong, *Nat. Commun.*, 2021, **12**, 1256.
- J. Xu, Y. Wang, S. Wu, Q. Yang, X. Fu, R. Xiao and H. Li, *ACS Appl. Mater. Interfaces*, 2023, **15**, 21086–21096.
- B. Tao, D. Zhong, H. Li, G. Wang and H. Chang, *Chem. Sci.*, 2023, **14**, 8693–8722.
- S. Bandyopadhyay and B. Nandan, *Mater. Today Energy*, 2023, **31**, 101201.
- Q. Zhao, S. Stalin, C. Z. Zhao and L. A. Archer, *Nat. Rev. Mater.*, 2020, **5**, 229–252.
- M. Armand and J. M. Tarascon, *Nature*, 2008, **451**, 652–657.
- Q. Ma and F. Tietz, *ChemElectroChem*, 2020, **7**, 2693–2713.
- H. Ahmad, K. T. Kubra, A. Butt, U. Nisar, F. J. Iftikhar and G. Ali, *J. Power Sources*, 2023, **581**, 233518.
- N. Aslfattahi, L. Samylingam, M. S. Kiai, K. Kadirkama, V. Kulish, M. Schmirler and Z. Said, *J. Energy Storage*, 2023, **72**, 108781.
- B. A. Goldmann, M. J. Clarke, J. A. Dawson and M. S. Islam, *J. Mater. Chem. A*, 2022, **10**, 2249–2255.
- J. Zhu, Y. Wang, S. Li, J. W. Howard, J. Neufeind, Y. Ren, H. Wang, C. Liang, W. Yang, R. Zou, C. Jin and Y. Zhao, *Inorg. Chem.*, 2016, **55**, 5993–5998.
- J. Liang, X. Li, S. Wang, K. R. Adair, W. Li, Y. Zhao, C. Wang, Y. Hu, L. Zhang, S. Zhao, S. Lu, H. Huang, R. Li, Y. Mo and X. Sun, *J. Am. Chem. Soc.*, 2020, **142**, 7012–7022.
- L. Van Duong, M. T. Nguyen and Y. A. Zulueta, *RSC Adv.*, 2022, **12**, 20029–20036.
- K.-H. Park, K. Kaup, A. Assoud, Q. Zhang, X. Wu and L. F. Nazar, *ACS Energy Lett.*, 2020, **5**, 533–539.
- E. Sebti, J. Qi, P. M. Richardson, P. Ridley, E. A. Wu, S. Banerjee, R. Giovine, A. Cronk, S.-Y. Ham, Y. S. Meng, S. P. Ong and R. J. Clément, *J. Mater. Chem. A*, 2022, **10**, 21565–21578.
- W. G. Zeier, R. Schlem, A. Banik, M. Eckardt and M. Zobel, *ACS Appl. Energy Mater.*, 2020, **3**, 10164–10173.
- L. Wang, Z. Song, X. Lou, Y. Chen, T. Wang, Z. Wang, H. Chen, W. Yin, M. Avdeev, W. H. Kan, B. Hu and W. Luo, *Small*, 2024, 2400195.
- Y. A. Zulueta and M. T. Nguyen, in *Annual Reports in Computational Chemistry*, Elsevier, 2023, vol. 19, pp. 1–43.



24 Y. A. Zulueta and M. T. Nguyen, *Phys. Chem. Chem. Phys.*, 2023, **25**, 27926–27935.

25 A. A. Franco, A. Rucci, D. Brandell, C. Frayret, M. Gaberscek, P. Jankowski and P. Johansson, *Chem. Rev.*, 2019, **119**, 4569–4627.

26 H. J. Lee, B. Darminto, S. Narayanan, M. Diaz-Lopez, A. W. Xiao, Y. Chart, J. H. Lee, J. A. Dawson and M. Pasta, *J. Mater. Chem. A*, 2022, **10**, 11574–11586.

27 Y. A. Zulueta, M. P. Pham-Ho and M. T. Nguyen, *J. Phys. Chem. Solids*, 2024, **188**, 111916.

28 M. C. Payne, M. P. Teter, D. C. Allan, T. A. Arias and J. D. Joannopoulos, *Rev. Mod. Phys.*, 1992, **64**, 1045–1097.

29 D. Vanderbilt, *Phys. Rev. B: Condens. Matter Mater. Phys.*, 1990, **41**, 7892–7895.

30 H. J. Monkhorst and J. D. Pack, *Phys. Rev. B: Solid State*, 1976, **13**, 5188–5192.

31 J. D. Gale and A. L. Rohl, *Mol. Simul.*, 2003, **29**, 291–341.

32 Computational Modelling of Zinc Oxide and Related Oxide Ceramics, University of Surrey, <https://openresearch.surrey.ac.uk/esploro/outputs/doctoral/Computational-Modelling-of-Zinc-Oxide-and-99512944702346>, accessed 30 December 2023.

33 B. G. Dick and A. W. Overhauser, *Phys. Rev.*, 1958, **112**, 90–103.

34 N. F. Mott and M. J. Littleton, *Trans. Faraday Soc.*, 1938, **34**, 485–499.

35 J. D. Gale, *J. Chem. Soc., Faraday Trans.*, 1997, **93**, 629–637.

36 L. L. Wong, K. C. Phuah, R. Dai, H. Chen, W. S. Chew and S. Adams, *Chem. Mater.*, 2021, **33**, 625–641.

37 S. Adams, *Solid State Ionics*, 2006, **177**, 1625–1630.

38 S. Adams and R. P. Rao, *Phys. Chem. Chem. Phys.*, 2009, **11**, 3210–3216.

39 I. D. Brown, *Chem. Rev.*, 2009, **109**, 6858–6919.

40 H. Chen, L. L. Wong and S. Adams, *Acta Crystallogr.*, 2019, **75**, 18–33.

41 F. A. Kröger, *The Chemistry of Imperfect Crystals*, North-Holland Pub. Co., 1964.

42 M. G. Medvedev, I. S. Bushmarinov, J. Sun, J. P. Perdew and K. A. Lyssenko, *Science*, 2017, **355**, 49–52.

43 Z. Ding, J. Li, J. Li and C. An, *J. Electrochem. Soc.*, 2020, **167**, 070541.

44 X. Ke, Y. Wang, G. Ren and C. Yuan, *Energy Storage Mater.*, 2020, **26**, 313–324.

45 M. Hou, F. Liang, K. Chen, Y. Dai and D. Xue, *Nanotechnology*, 2020, **31**, 132003.

46 M. Born, K. Huang and M. Lax, *Am. J. Phys.*, 1955, **23**, 474.

47 F. Mouhat and F. X. Coudert, *Phys. Rev. B: Condens. Matter Mater. Phys.*, 2014, **90**, 224104.

48 I. N. Frantsevich, F. F. Voronov and S. A. Bokuta, *Elastic Constants and Elastic Moduli of Metals and Insulators Handbook*, Naukova Dumka, Kiev, 1983, pp. 60–180.

49 F. I. Fedorov, *Theory of Elastic Waves in Crystals*, Springer US, Boston, MA, 1968.

50 W. Voigt, *Lehrbuch der Kristallphysik*, BG Teubner, Leipzig und 791 Berlin, 980 S, Reproduced 1966 Spring Fachmedien Wiesbaden GmbH, 1928.

51 A. Reuss, *Z. Angew. Math. Mech.*, 1929, **9**, 49–58.

52 R. Hill, *Proc. Phys. Soc., London, Sect. A*, 1952, **65**, 349–354.

53 R. Hill, *J. Mech. Phys. Solids*, 1963, **11**, 357–372.

54 S. F. Pugh, *London, Edinburgh Dublin Philos. Mag. J. Sci.*, 1954, **45**, 823–843.

